OPEN ACCESS

Inorganic Materials ARTICLE

The Innovation Materials

Universal Taxol molecular binding engineering in dual-polarity MoS_2 photodetector

Yongkang Jiang,[1,5] YuSheng Xie,[1,5] Qiming Pan,[1,5] Jinping Li,[1,5] Qi Zhan,[1] Yujie Sun,[1] JinShan Wang,[2] Yang Ren,[2,*] Xinghong Wang,[3] Kenan Zhang,[4,*] and Feng Qiu[1,*]

*Correspondence: fengqiu@ynu.edu.cn (F.Q.); reny@ynu.edu.cn (Y.R.); kenzhang@mit.edu (K.Z.)

Received: June 11, 2025; Accepted: January 7, 2026; Published Online: January 16, 2026; https://doi.org/10.59717/j.xinn-mater.2026.100191

GRAPHICAL ABSTRACT

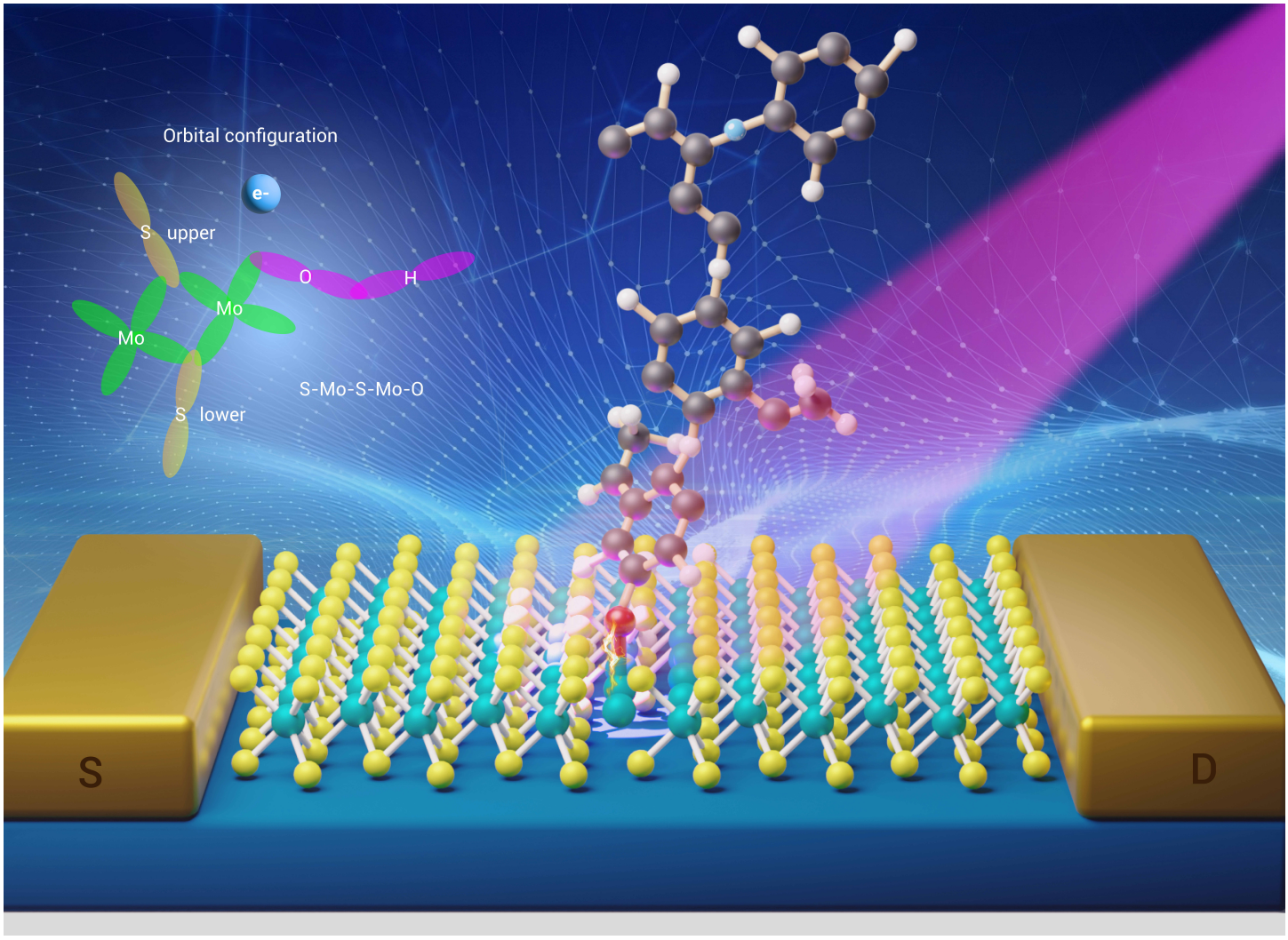

PUBLIC SUMMARY

- Taxol molecules hold considerable potential for enhancing the optoelectronic performance of 2D materials.
- Taxol can effectively passivate the interfacial defects of MoS_2 while preserving its crystalline integrity.
- Establishing interfacial Mo-O bonding pathways enables directional electron transfer.
- Taxol modification strategy enables increased carrier mobility and reduced electronic noise.

ARTICLE Inorganic Materials

OPEN ACCESS

Universal Taxol molecular binding engineering in dual-polarity MoS_2 photodetector

Yongkang Jiang,[1,5] YuSheng Xie,[1,5] Qiming Pan,[1,5] Jinping Li,[1,5] Qi Zhan,[1] Yujie Sun,[1] JinShan Wang,[2] Yang Ren,[2,*] Xinghong Wang,[3] Kenan Zhang,[4,*] and Feng Qiu[1,*]

[1]National Center for International Joint Research of Photoelectric Energy Materials and Application, Yunnan Key Laboratory of Electromagnetic Materials and Devices, School of Materials and Energy, Yunnan University, Kunming 650500, China

[2]School of Physics and Astronomy, Yunnan University, Kunming 650500, China

[3]Yunnan Institute of Microbiology, Yunnan University, Kunming 650500, China

[4]Department of Electrical Engineering and Computer Science, Massachusetts Institute of Technology, Cambridge 02139, USA

[5]These authors contributed equally

*Correspondence: fengqiu@ynu.edu.cn (F.Q.); reny@ynu.edu.cn (Y.R.); kenzhang@mit.edu (K.Z.)

Received: June 11, 2025; Accepted: January 7, 2026; Published Online: January 16, 2026; https://doi.org/10.59717/j.xinn-mater.2026.100191

Citation: Jiang Y., Xie Y., Pan Q., et al. (2026). Universal Taxol molecular binding engineering in dual-polarity MoS_2 photodetector. *The Innovation Materials* **4**:100191.

Intrinsic defects in two-dimensional (2D) atomic crystals impose severe constraints on carrier utilization through defect-induced trapping and recombination. While surface modification and mobility recovery strategies have been widely explored, the development of a universal defect mitigation protocol remains unresolved. Here, we introduce a molecular passivation strategy in which Taxol molecules, via their hydroxyl radicals, repair intrinsic sulfur vacancies in monolayer MoS_2, thereby markedly accelerating carrier transport dynamics. The Taxol framework not only modulates the electronic structure of n-type MoS_2 lattices but also shows compatibility with p-type MoS_2 configurations, enabling robust interfacial unit cell binding. Following modification, both n- and p-type MoS_2 exhibit acoustic phonon-limited mobilities enhanced and more than an order of magnitude for p-type conuterpart. This universal lattice-reconstruction strategy further suppresses noise power by up to six orders of magnitude and restrain interface state, while achieving a responsivity above 200 A W^{-1} and specific detectivity exceeding 1.0×10^{12} Jones — representing an improvement of four orders of magnitude. Complementary theoretical calculations confirm that Taxol-mediated coordination effectively passivates sulfur vacancies and optimizes charge transport. These findings establish a universal molecular coordination protocol to mitigate defect-related noise currents and boost detection sensitivity, advancing the performance of 2D photodetectors for next-generation optoelectronic and biosensing applications.

INTRODUCTION

As a representative transition metal dichalcogenides (TMDs), molybdenum disulfide (MoS_2) possesses a tunable bandgap and high specific surface area,[1,2] making it a promisingwith an argon flow of 200 sccm candidate for next-generation optoelectronic devices.[3-7] However, intrinsic structural defects,[8,9] particularly sulfur vacancies, act as recombination centers that markedly degrade photoelectric performance. Consequently, effective defect passivation has emerged as a central challenge in the advancement of MoS_2-based photodetectors.[10] Lattice-binding engineering and organic molecule surface modification have shown synergistic potential for repairing defects and enhancing optoelectronic properties.[11-18] Conventional passivation strategies — including vacancy repair,[19] lattice substitution,[20] antisite defect engineering,[21] adatom incorporation, and grain boundary modulation,[22,23] have demonstrated efficacy. However, establishing a universal strategy capable of modulating both n-type and p-type 2D materials remains difficult. This challenge is particularly pronounced for monolayer MoS_2 (1L-MoS_2), where the absence of dangling bonds and limited supramolecular interactions make surface modifications more complex and less controllable.[5,24]

Molecular modification strategies for TMDs include thermal evaporation, solution spin coating,[25-27] drop casting,[28,29] and soaking.[30-32] In these approaches, target small molecules or polymers are typically immobilized on the TMD surface through physisorption.[33] Strong electron-donating or -withdrawing organic molecules can facilitate electron transfer or migration, thereby tuning the electronic properties of TMDs.[34] For instance, hydroxyl radical (-OH) adsorption on monolayer MoS_2 introduces intermediate gap states that facilitate edge reconstruction, while catechol and 1,10-phenanthroline provide stable n-doping.[35] Likewise, sub-nanocluster modifications with Pd, Ru, and PdRu alloys regulate photogenerated carriers, extending the spectral range of photodetection.[36] Nevertheless, these strategies typically rely on the physical deposition of organic molecules and rarely establish specific interfacial interactions. Taxol (paclitaxel) — a complex organic molecule widely used as an anticancer drug — presents unique advantages,[37,38] including high chemical stability, biocompatibility, multiple functional groups (e.g., hydroxyl and ester), and strong UV absorption.[39] The development of taxol-based biosensing platforms capable of detecting ultra-low-abundance cancer biomarkers has generated considerable impetus for targeted therapeutics and molecular diagnostics. Nevertheless, realizing such biosensors remains challenging the limited fidelity of molecular recognition and the inefficiency of signal transduction. Importantly, the conjugated structure of Taxol is highly relevant for materials engineering: it enables strong π-π interactions, efficient charge transfer, geometric adaptability to defect sites, and chemical stability. These attributes position Taxol as a promising candidate for defect healing and optoelectronic enhancement in MoS_2-based materials. Yet, despite this potential, applications of Taxol in optoelectronic systems remain largely unexplored, leaving Taxol/MoS_2 composite platforms as an open frontier for future research.

Here, we propose a universal defect passivation strategy based on interfacial modification of monolayer MoS_2 using Taxol molecules. N-type and p-type MoS_2 were synthesized via molten salt-assisted Chemical Vapor Deposition (CVD) and sputtering-CVD two-step method.[40,41] The as-fabricated Field-Effect Transistors (FETs) exhibited low mobility and poor photoelectric performance due to inherent defects. Following Taxol modification, the noise power spectral density was reduced by 2-5 orders of magnitude, accompanied by significant improvements in mobilities and detectivities. Theoretical and experimental results all reveal that hydroxyl groups in Taxol form bonds with Mo atoms, facilitating electron transfer and effectively passivating defects without disrupting the MoS_2 lattice. These findings demonstrate the feasibility of employing organic molecules for defect engineering in transition metal dichalcogenides and highlight the synergistic enhancement of optoelectronic performance in Taxol-modified MoS_2 photodetectors.

MATERIALS AND METHODS

Material fabrication and composite formation

SiO_2 (300 nm)/Si was used as the growth substrate, cut into 1.5 × 1 cm^2 rectangular pieces. The substrates were cleaned in acetone, ethanol, and deionised water for 16 minutes each and then dried with nitrogen gas. For the molten salt-assisted chemical vapor deposition (CVD) method, a quartz boat containing sulfur powder (≥ 99.5%, Sigma-Aldrich) was placed in the low-temperature upstream zone at approximately 200°C. Another quartz boat, with 3 mg of MoO_3 powder (≥ 99.5%, Sigma-Aldrich) mixed with 0.1 mg of NaCl at the front and the substrate placed upside down at the back, was positioned in the high-temperature central zone of the furnace. Before growth, the furnace pressure was reduced to 4×10^{-2} mbar and purged with 500 sccm of argon gas (99.99% purity) to remove residual contaminants. During growth, high-purity (99.99%) argon served as the carrier gas at a flow rate of 200 sccm, with the pressure maintained at 2×10^2 mbar. The temper-

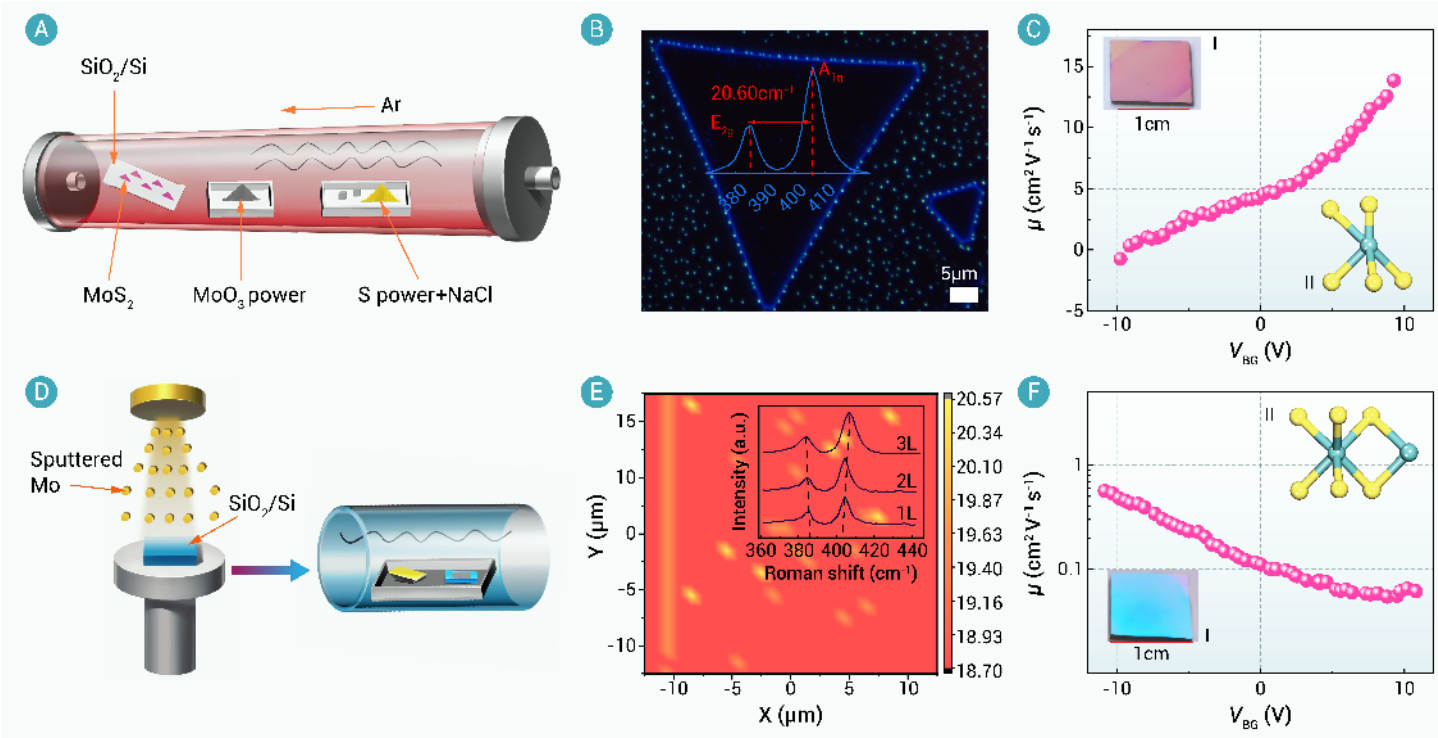

Figure 1. Growth and characterisation of MoS_2 films (A-C) Molten salt-assisted CVD Growth: (A) Schematic illustration of the growth process. (B) Dark-field optical image of triangular MoS_2 crystals, with the corresponding Raman spectrum shown in the inset. (C) Mobility spectrum of n-type MoS_2, with inset I showing an optical image of the MoS_2 film and inset II depicting the atomic structure of n-type MoS_2. (D-F) Sputtering-CVD two-step growth: (D) Schematic illustration of the two-step growth process. (E) Raman mapping with the corresponding Raman spectrum shown in the inset. (F) Mobility spectrum of p-type MoS_2, with inset I showing an optical image of the sputtered Mo film and inset II depicting its atomic structure.

ature in the high-temperature zone was ramped to 750°C over 63 minutes, while the low-temperature zone was heated to 200°C over 20 minutes. The system was maintained at the growth temperature of 750°C for 5-15 minutes. For the sputtering-CVD two-step method, a 300 nm SiO_2/Si substrate was used, ultrasonically cleaned, and transferred to the vacuum chamber of the magnetron sputtering system. Chamber pressure was reduced to 1×10^{-6} mTorr using molecular and mechanical pumps. Mo thin films were deposited at a sputtering pressure of 1 Pa with an argon flow rate of 20 sccm. In the second step, the Mo thin films were sulfurised in a tube furnace. The furnace was initially evacuated to 4×10^{-2} mbar, and argon was introduced, followed by three cycles of gas purging to remove air thoroughly. The centre of the tube was heated to 750°C with an Ar flow of 200 sccm and a chamber pressure of 2×10^{2} mbar. To fabricate the Taxol/MoS_2 composite, a solution of Taxol dissolved in methanol was applied to the MoS_2 film surface using a pipette. When methanol evaporated, Taxol crystallized and deposited on MoS_2 surface. The sample was then placed in a vacuum oven at 50°C overnight to obtain the Taxol/MoS_2 composite.

First-principle calculation methods

The first-principles calculations were conducted using the Density Functional Theory (DFT)[42] within the Vienna Ab initio Simulation Package (VASP).[43,44]The Projector Augmented Wave (PAW)[45] method accounted for electron-core interactions via pseudopotentials. The exchange-correlation function is a Generalized Gradient Approximation Perdew-Burke-Ernzerhof (GGA-PBE).[46] A semiclassical dispersion correction scheme (DFT-D3)[47] was employed to include the effects of long-range vdW interactions. The cutoff energy of 450 eV was set to determine the size of the plane-wave basis set. The k-point mesh is set to 9 × 9 × 1. The convergence criterion is reached when the energy on each atom is less than 1.00×10^{-6} eV and the force on each atom is less than 0.01 eV/Å. During the construction of the computational model, a vacuum layer of 20 Å in thickness was added on top of the monolayer MoS_2 (4 × 4 × 1) to avoid interaction between layers. In the adsorption model, the adsorption distance of OH is controlled at 1.78 Å.[48] The adsorption energy (E_{ads}) was defined as:

$$E_{ads} = E_{tot}(\text{adsorbate/MoS}_2) - E_{tot}(\text{MoS}_2) - E_{tot}(\text{adsorbate}) \quad (1)$$

where E_{tot} (MoS_2), E_{tot} (adsorbate), and E_{tot} (adsorbate/MoS_2) represent the total energy for the MoS_2, adsorbate, and OH-adsorbed MoS_2, respectively. In addition, the deformation potential theory employed in this work was proposed by Bardeen and Shockley in 1950.[49] In this theory, the local deformation induced by acoustic lattice waves is regarded as equivalent to that in a uniform crystal, and the effective potential arising from long-wavelength acoustic waves is termed the deformation potential. When the energy of acoustic phonons in the long-wavelength limit is negligible compared to the electron energy, the scattering is treated as elastic and acts as a perturbation to the electrons in the lattice. This perturbation can be described by a mathematical expression involving elastic constants and lattice deformation. Based on this theory, the carrier mobility in two-dimensional materials can be expressed as:

$$\mu = \frac{2e\hbar^3 C_{ij}}{3k_B T|m^*|^2 E_1^2} \quad (2)$$

where e, $\hbar$, k_B, T, m^*, E_1, and C_{ij} are the elementary charge, reduced Planck constant, Boltzmann constant, temperature, effective mass, deformation-potential constant, and elastic constant, respectively.

Characterization and measurement

The dark-field imaging of triangular MoS_2 single crystals was observed using a fluorescence microscope (Metatest, E3-iFL). Film thickness was measured in air using an atomic force microscope (Seiko SPI-3800). Raman/photoluminescence (PL) measurements were conducted at room temperature using a Raman spectrometer (Renishaw in Via Reflex) with 532 nm laser excitation at a laser intensity of 5%. X-ray photoelectron spectroscopy (XPS) analysis was performed using an X-ray diffractometer (SmartLab SE) in a vacuum of 10-10 mbar to calibrate the C 1s spectrum and determine the chemical composition of elements such as Mo and S. The morphology and microstructure of Taxol/MoS_2 were analysed using a field-emission scanning electron microscope (Zeiss Gemini 500). A two-dimensional transfer system (Metatest, E1-T) was used to apply a mask for elec-

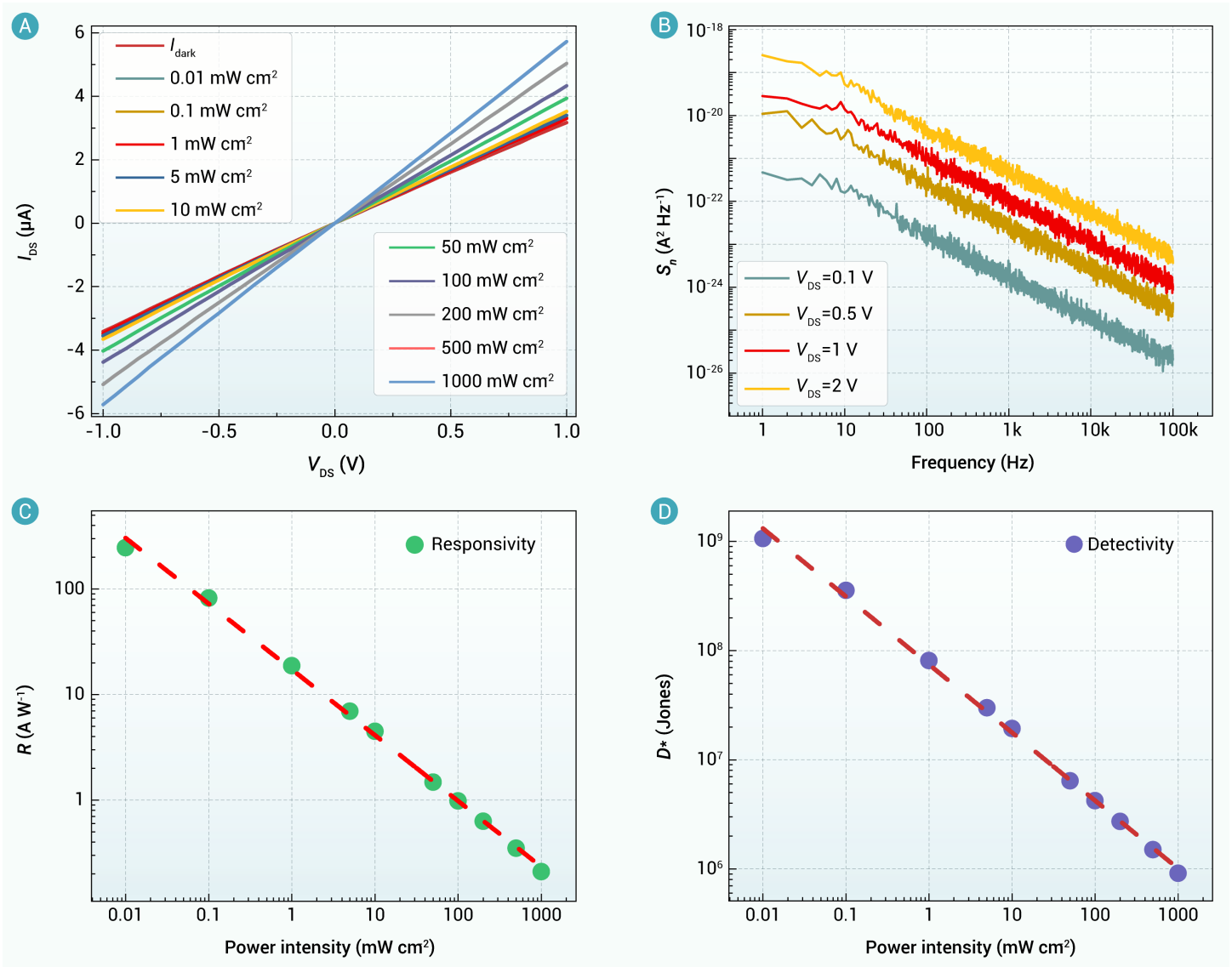

Figure 2. Optoelectronic performance of n-MoS_2 photodetectors prepared by one-step method (A) I_{DS}-V_{DS} curves of n-MoS_2 FETs under different optical power densities. (B) Noise current power spectral density as a function of frequency at different V_{DS}. (C) Responsivity of the device under different optical power densities. (D) Detectivity of the device under different optical power densities.

trode positioning, followed by placement in a high-vacuum evaporation system (HZ-300) to deposit 150 nm thick Ag electrodes. The electrical and optical properties of the devices were evaluated in air at room temperature using a semiconductor parameter analyzer (PRIMARIUS Fs-Pro) and a 405 nm laser. Noise power spectrum was recorded by a Noise Measurement System (PRIMARIUS Fs-Pro, 100 kHz bandwidth).[50,51]

RESULTS AND DISCUSSION

To investigate the modification effects of Taxol on MoS_2, n-type and p-type MoS_2 were synthesized using molten salt-assisted CVD and sputtering-CVD methods, respectively. Figure 1A presents the schematic of MoS_2 growth via molten salt-assisted CVD. In this process, NaCl was employed as a seed promoter, while precursor concentration, growth pressure, carrier-gas flow rate, and growth time were systematically optimized to regulate nucleation and crystal growth (see Experimental Section). This strategy enabled the fabrication of large triangular MoS_2 single crystals with edge length ~150 μm. By extending the growth time, continuous high-quality, large-area MoS_2 films were obtained (Figure S1). Figure 1B displays a representative optical micrograph of a triangular MoS_2 single-crystal. Raman spectroscopy, a nondestructive probe for layer determination, confirmed the structural characteristics.[52] The spectrum (inset) reveals the in-plane (E^1_{2g}) and out-of-plane (A_{1g}) vibrational modes at 385.28 cm^{-1} and 405.91 cm^{-1}, respectively, with a frequency separation (Δk) of 20.60 cm^{-1}, which is consistent with the single-layer spectral range.[53]

To further validate the quality and layer number of the MoS_2 films, atomic force microscopy (AFM), Raman mapping, and photoluminescence (PL) spectroscopy were performed in Figures S2A-B. AFM measurements revealed a thickness of ~0.75 nm, consistent with monolayer MoS_2 on SiO_2/Si matrix.[54] The PL spectrum exhibited a pronounced exciton peak (A line), characteristic of the direct bandgap of monolayer MoS_2.[8] Collectively, these results confirm the successful fabrication of large-area monolayer MoS_2. Figure 1C presents the mobility spectrum, demonstrating that the MoS_2 grown by molten salt-assisted CVD exhibits n-type semiconductor. Insets I and II display the optical micrograph of the MoS_2 film grown on a SiO_2/Si substrate and the corresponding atomic model of n-type MoS_2, respectively.

Large-area MoS_2 films were also fabricated using a sputtering-CVD two-step method. As illustrated in Figure 1D, magnetron sputtering was first used to deposit Mo films of controlled thickness onto Si/SiO_2 substrates, followed by sulfurization in a CVD tube furnace. Although achieving a fully uniform monolayer of MoS_2 across the entire substrate remains challenging, Raman mapping of the E^1_{2g}-A_{1g} frequency difference (Δk) over a 25 μm × 25 μm area (Figure 1E) reveals good uniformity, with an average Δk of 18.77 cm^{-1}, consistent with exfoliated MoS_2,[55] confirming that the film is predominantly monolayer with 17.4 ≤ Δk ≤ 20.6.[41] The Mo film thickness can be precisely

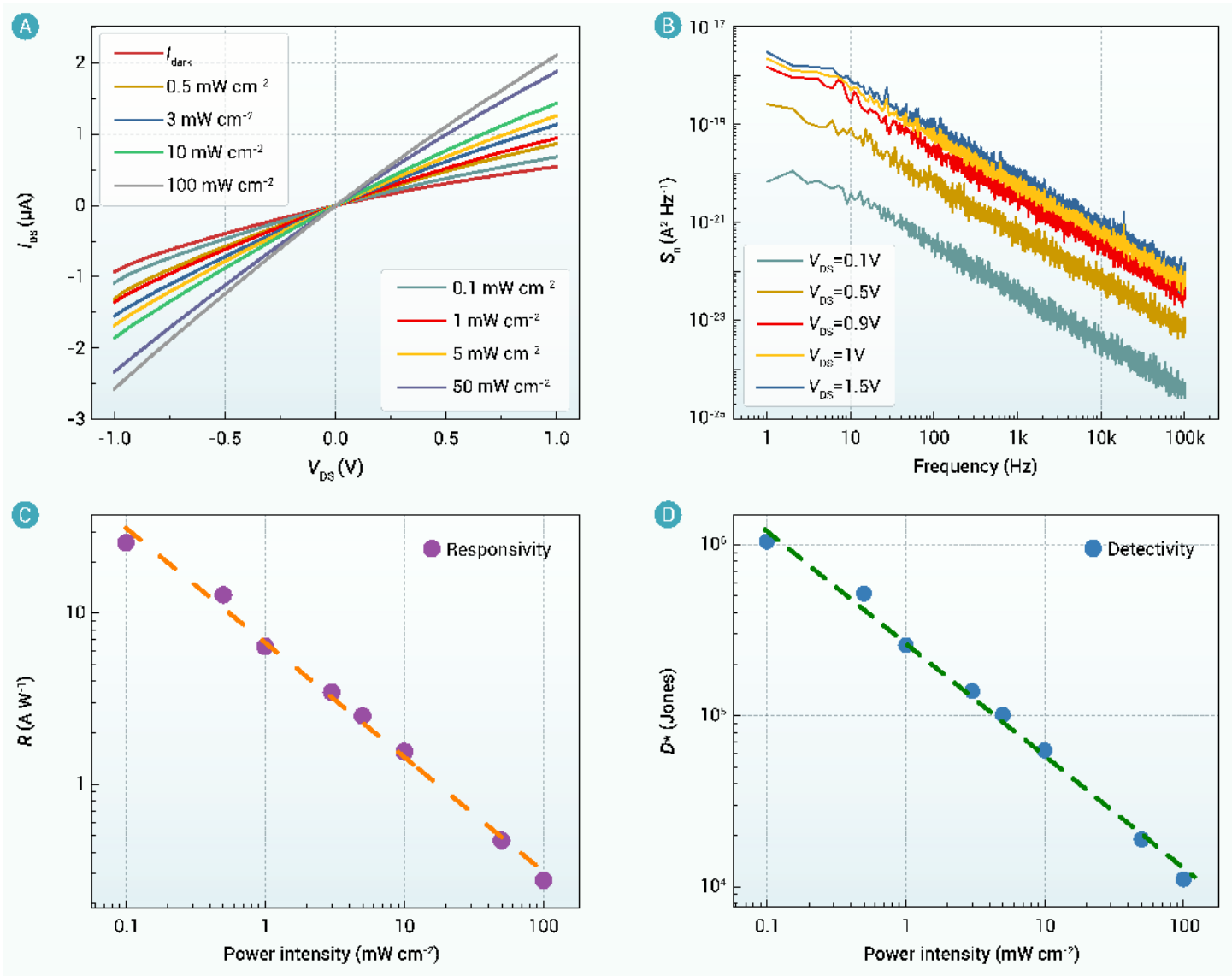

Figure 3. Optoelectronic performance of p-MoS_2 photodetectors prepared by two-step method (A) I_{DS}-V_{DS} curves of p-MoS_2 FETs under different optical power densities. (B) Noise current power spectral density as a function of frequency at different V_{DS}. (C) Responsivity of the device under different optical power densities. (D) Detectivity of the device under different optical power densities.

tuned by adjusting the Radio Frequency (RF) sputtering power, enabling subsequent sulfurization to yield MoS_2 films with controllable layer numbers. To further verify the uniformity and crystallinity of the MoS_2 films, we employed a variety of characterization techniques including SEM, Raman multi-point testing, and XRD. The characterization results shown in Figure S3 clearly demonstrate that the MoS_2 films prepared in this study exhibit excellent uniformity and crystallinity.

Figure S4A schematically compares the thicknesses of Mo andMoS_2 films, demonstrating the efficiency of the sputtering-CVD method for scalable fabrication. With increasing thickness, both characteristic peaks shift, leading to larger Δk values. Figure S4B shows the PL spectra of MoS_2 films with varying thicknesses. The monolayer exhibits the strongest PL intensity due to efficient electron-hole recombination. As the number of layers increases, however, interlayer coupling and the transition to an indirect bandgap suppress exciton recombination efficiency, diminishing the PL intensity. The mobility measurement (Figure 1F) further confirms that the MoS_2 produced via this method exhibits p-type characteristics. Insets I and II show an optical image of large-area Mo films and the corresponding atomic model of p-type MoS_2, respectively. Additional analyses of the molecular features (Figures S5-S6) verify the successful integration of Taxol/MoS_2, demonstrating the effective assembly of the composite.

Building on the successful fabrication of the Taxol/MoS_2 composite, this study proceeded to explore its effect on optoelectronic device performance. Back-gated field-effect transistors were first fabricated on both n- and p-type MoS_2 thin films. These devices underwent systematic electrical and optical characterization (Figures 2-3), establishing a baseline for subsequent comparison.

Figure 2 summarizes the optoelectronic performance of the n-type MoS_2 (n-MoS_2) employed in this work. Specifically, Figure 2A presents the current-voltage (I_{DS}-V_{DS}) characteristics of the n-MoS_2 device, which were recorded under 405 nm illumination with varying power densities. Figure 2B shows the noise power spectral density of the n-MoS_2 device measured in the dark, with data collected at different bias voltages. Meanwhile, Figures 2C-D display two key performance metrics — responsivity (R) and specific detectivity (D^*) — of the n-MoS_2 device, plotted as functions of incident power density. R and D^* are calculated using the following equations:[56,57]

$$R = \frac{I_{ph}}{PA} \tag{3}$$

$$D^* = \frac{\sqrt{A \cdot \Delta f}}{NEP} = \frac{R\sqrt{A \cdot \Delta f}}{\overline{i_n^2}^{1/2}} = \frac{R\sqrt{A \cdot \Delta f}}{\sqrt{\int_0^{\Delta f} S_n df}} = \frac{R\sqrt{A \cdot \Delta f}}{\sqrt{S_1(\ln \Delta f + 1)}} = \frac{R\sqrt{A}}{\sqrt{S_1}} \tag{4}$$

where I_{ph} is the photocurrent, P is the incident light power, A is the real light-

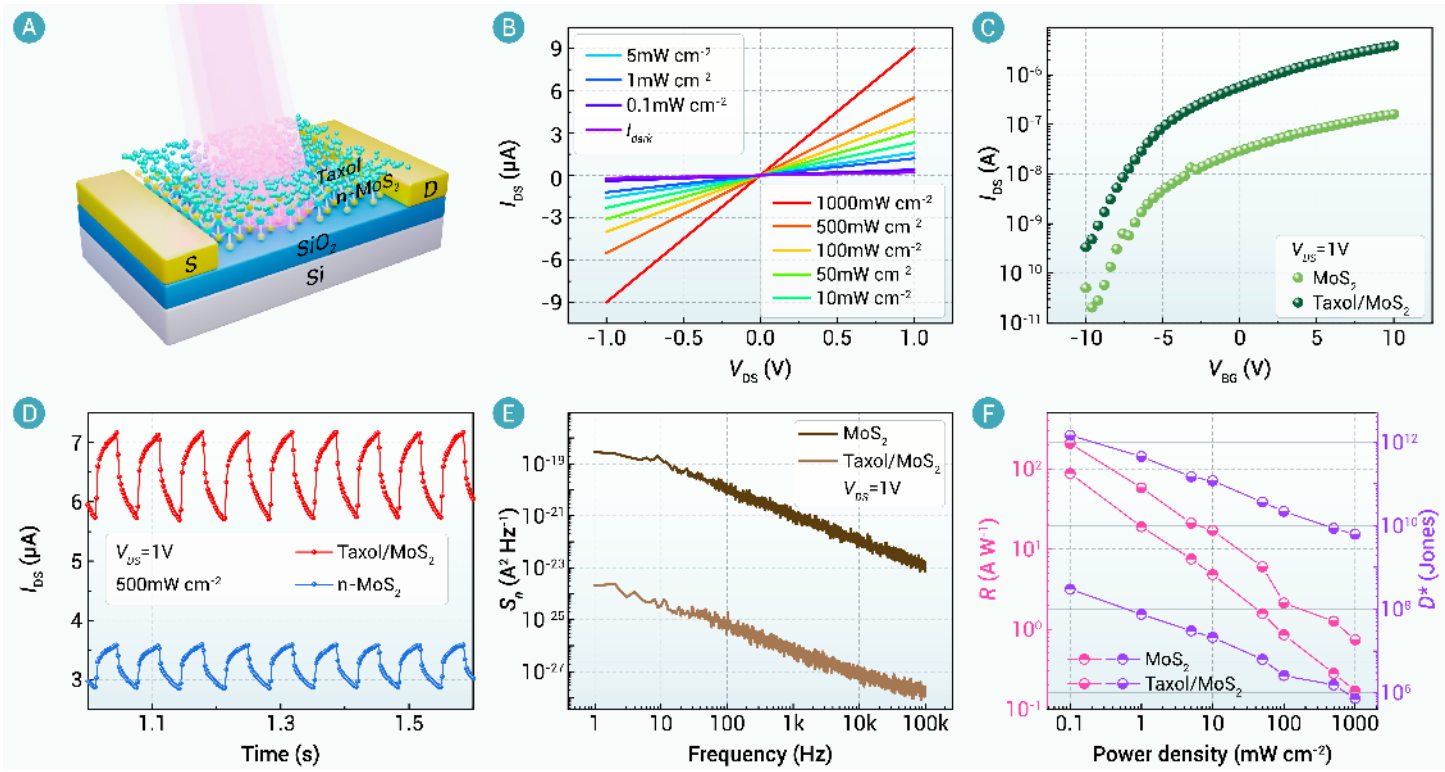

Figure 4. Photodetection performance of n-MoS_2 FETs before and after Taxol modification (A) Schematic illustration of Taxol/n(p)-MoS_2 FET. (B) Output curves (I_{DS}-V_{DS}) of the Taxol/n-MoS_2 FET under different incident light power densities. (C) Transfer characteristics (V_{DS} = 1 V), demonstrating the enhanced field-effect behavior for the Taxol/MoS_2 FET. (D) Time-dependent photoresponse (V_{DS} = 1 V) under 405 nm laser illumination with a light power density of 10 mW cm^{-2}. (E) Noise power spectral density as a function of frequency (V_{DS} = 1 V). (F) Responsivity (R) and specific detectivity (D^*) plotted against light power density (V_{DS} = 1 V).

absorbing area of the detector active region, Δf is the noise equivalent bandwidth (Δf = 1), NEP is noise equivalent power; S_n is the noise power spectral density,[58,59] and S_I represents the noise power spectra at 1Hz. There are critical metrics for evaluating photodetector performance. At an ultralow irradiance of 0.01 mW cm^{-2}, this n-MoS_2 device achieves a peak responsivity of 305 A W^{-1} and a specific detectivity of 1.31 × 10^9 Jones.

Figure 3 corresponds to the optoelectronic performance of the p-type MoS_2 (p-MoS_2) in this work, following a similar subfigure layout to Figure 2 for direct comparability. Figure 3A shows the I_{DS}-V_{DS} characteristics of the p-MoS_2 device under 405 nm illumination (with varying power densities), and Figure 3B presents its noise power spectral density measured in the dark (at different bias voltages). Figures 3C-D further display the responsivity and specific detectivity of the p-MoS_2 device as functions of incident power density. For the p-MoS_2 device, the peak performance occurs at an ultralow irradiance of 0.1 mW cm^{-2}, where it attains a responsivity of 31.5 A W^{-1} and a specific detectivity of 1.04 × 10^6 Jones.

Taxol was subsequently incorporated into n-MoS_2 FETs (Figure 4A), enabling a detailed investigation of its interface effects on device performance. Firstly, the modification of Taxol molecules on MoS_2 films is examined. Following hybridization, the I_{DS}-V_{DS} curves (Figure 4B) under various light power densities with 405 nm laser irradiation exhibited symmetric and linear behavior, indicative of high-quality ohmic contacts. The device achieved a saturation current of 9 μA at V_{DS} = 1 V, confirming a pronounced enhancement in photoresponse.

The transfer curves exhibit an n-type behavior for both the MoS_2 and Taxol/MoS_2 FETs (Figure 4C). The field-effect mobility can be calculated using the following formula:[60]

$$\mu = \frac{d(I_{DS})}{d(V_G)} \times \frac{L}{W} \times \frac{1}{C_O V_{DS}} \quad (5)$$

where $\frac{d(I_{DS})}{d(V_G)}$ represents the slope of the drain current I_{DS} versus the gate voltage V_G, L and W are the channel length and width, respectively, I_{DS} is the current between the drain and source terminals, C_O is the capacitance of the gate dielectric, and V_{DS} is the source-drain voltage. The field-effect mobility for the n-MoS_2 FET was calculated to be 13.8 cm^2 V^{-1} s^{-1} using Equation (5), while the Taxol/n-MoS_2 FET achieved a significantly improved mobility of 19.9 cm^2 V^{-1} s^{-1}, attributed to the reduced interface defects and improved current conduction capacity. Figure 2D shows the time-dependent photoresponse at V_{DS} = 1 V under a light power density of 10 mW cm^{-2}. The Taxol/n-MoS_2 FET exhibits higher photocurrent and faster charge transport compared to unmodified n-MoS_2, suggesting that the hybridisation with Taxol improves light absorption and photoelectric conversion efficiency, significantly enhancing the photoresponse.

Figure 4E shows that at V_{DS} = 1 V, the noise power spectral density exhibits typical frequency-dependent 1/f noise characteristics. In this figure, the noise power density spectrum of n-MoS_2 at 1 Hz is 2.83 × 10^{-19} A^2 Hz^{-1}, while the noise power density spectrum of taxol-modified Taxol/n-MoS_2 at 1 Hz is 2.08 × 10^{-24} A^2 Hz^{-1}. After Taxol modification, the noise power spectral density of the n-MoS_2 FET decreased by five orders of magnitude, reflecting a substantial reduction in interface defects and trap states. This suppression of carrier scattering and recombination is directly associated with the enhanced mobility and overall device performance. According to the McWhorter model, the interface state D_{it}, was extracted from the 1/f noise measurement via the following equation:[61]

$$\frac{S_n}{I_{ds}^2} = \left(\frac{g_m}{I_{ds}}\right)^2 S_{vfb} \quad (6)$$

$$S_{vfb} = \frac{q^2 K_B T D_{it}}{W L C_{OX}^2 f} \quad (7)$$

where S_n is spectral density, g_m is the gate transconductance, S_{vfb} is the flat band voltage spectral density, q is the electronic charge, K_B is Boltzmann's constant, T is the temperature, W and L are the width and length of the channel, respectively, and C_{OX} is the gate capacitance per unit area. After Taxol modification, the D_{it} of the n-MoS_2 FET decreased from 2.43 × 10^{14} cm^{-2} eV^{-1} to 1.82 × 10^{11} cm^{-2} eV^{-1}, which approaches the interface state density requirement for International Roadmap for Devices and Systems (IRDS).[62] This further indicates that Taxol can effectively passivate defects in MoS_2. As

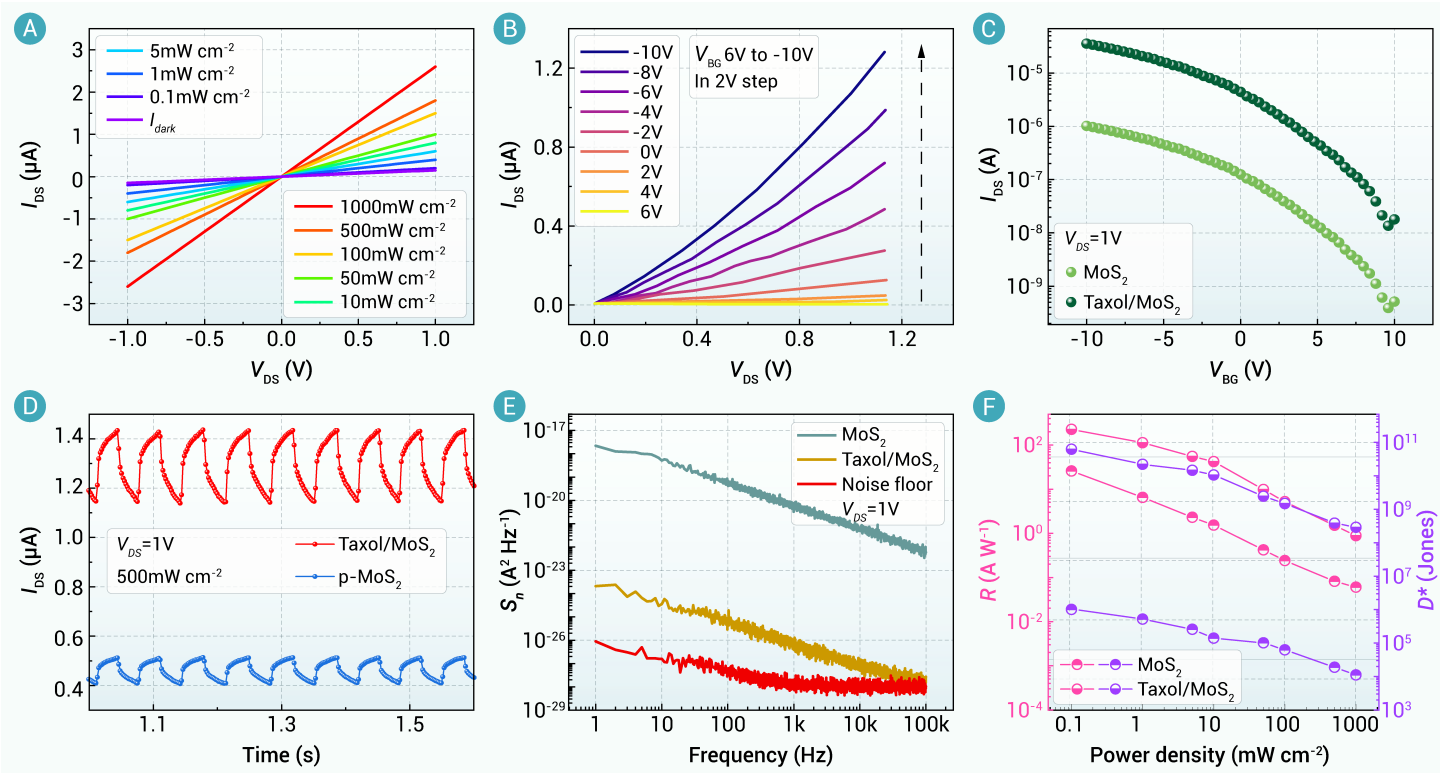

Figure 5. Photodetection performance of p-MoS_2 FETs before and after Taxol modification (A) I_{DS}-V_{DS} curves of the Taxol/p-MoS_2 FET under different light power densities. (B) Taxol/p-MoS_2 FET typical output (I_{DS}-V_{DS}) characteristics as a function of back-gate bias (V_{BG} = 6 V to -10 V, step size 2 V). (C) Transfer characteristics (V_{DS} = 1 V). (D) Time-dependent photoresponse (V_{DS} = 1 V, 405 nm laser) with light power density of 500 mW cm^{-2}. (E) Noise power spectral density at V_{DS} = 1 V. (F) Responsivity and detectivity as a function of light power density (V_{DS} = 1 V).

shown in Figure 4F, the Taxol/n-MoS_2 FET demonstrates significant improvements in both *R* and *D**. Based on the low noise current (1Hz) 1.44 × 10^{-12} A $Hz^{-1/2}$, the *R* increased from 88 A W^{-1} to 208 A W^{-1}, while the *D** rose from 3×10^8 Jones to 1.46 × 10^{12} Jones. These enhancements are particularly notable at lower light power densities, making the device highly suitable for low-light photodetection applications.

To further investigate the modification effect of Taxol on MoS_2 to demonstrate the general validity of their synergistic interaction, Taxol molecules were assembled on p-MoS_2 through van der Waals interactions. The device structure is largely consistent with that shown in Figure 4A. The output curves of the Taxol/MoS_2 FET under different light power densities, indicate good Ohmic contact and a pronounced increase in I_{DS} with rising light power density (Figure 5A). At V_{DS} = 1 V, the saturation current reaches 2.5 μA. The representative output characteristics and transfer curves (Figures 5B-C) of the Taxol/MoS_2 FET clearly confirm p-type semiconductor behavior. The field-effect mobility of the p-MoS_2 FET was calculated to be 0.42 cm^2 V^{-1} s^{-1}, whereas that of the Taxol/p-MoS_2 FET was markedly enhanced to 14.70 cm^2 V^{-1} s^{-1}.

In addition to enhancing the photoresponse (Figure 5D), Taxol modification substantially reduces the noise power spectral density by six orders of magnitude (Figure 5E)， For pristine p-type MoS_2 devices, the noise power spectral density at 1Hz is 2.19 × 10^{-18} A^2 Hz^{-1}, whereas Taxol/MoS_2 devices exhibit a reduced noise power spectral density of 2.08 × 10^{-24} A^2 Hz^{-1}, approaching the system itself noise floor at high frequent zone. This remarkable suppression is attributed to the π-system of Taxol, which injects additional holes into MoS_2 while simultaneously lowering the interfacial barrier, thereby facilitating faster and broader conduction channels for carrier extraction. Consequently, the extraction efficiency of photogenerated carriers and the external electron injection efficiency are both significantly improved.[63-67] Kinetically, Taxol modification shortens the photoresponse time: for p-MoS_2 FETs, the rise and fall times decrease from 380 to 250 ms and from 360 to 260 ms, respectively; for n-MoS_2 FETs, the rise and fall times decrease from 210 to 130 ms and from 220 to 180 ms, respectively. Meanwhile, the noise power spectral density is as low as 1 × 10^{-25} A^2 Hz^{-1}, yielding a 1/*f* noise corner frequency as low as 1 kHz. This extremely low noise level approaches the instrument's noise floor and is comparable to the lowest noise FETs reported in the literature,[68] underscoring the potential of this strategy for designing next-generation low-noise FETs. After Taxol functionalization, the D_{it} of the p-MoS_2 FET decreased from 1.88 × 10^{15} cm^{-2} eV^{-1} to 2.53 × 10^{11} cm^{-2} eV^{-1}, approaching the IRDS requirement of 10^{10} cm^{-2} eV^{-1} for low-standby-power CMOS.[62] Figure 5F further illustrates the enhancement in responsivity *R*, which increases from 25.83 A W^{-1} to 226.54 A W^{-1}, and specific detectivity *D**, which rises from 1.04 × 10^6 Jones to 6.25 × 10^{10} Jones. Overall, Taxol molecules provide an effective interfacial modification strategy that markedly improves the optoelectronic performance of both n- and p-type MoS_2 FETs.

To elucidate the mechanism underlying the enhanced photoresponse and noise suppression after Taxol modification on MoS_2, X-ray photoelectron spectroscopy (XPS) was performed on Taxol, MoS_2, and their composite system. Figure 6A shows the O 1s spectra before and after Taxol adsorption on MoS_2, revealing characteristic chemical state signals of C-OH, C=O-O, and C=O functional groups. To ensure effective adsorption, 10-deacetylated Taxol with reduced steric hindrance was employed, enabling intimate contact with MoS_2 surface. The peak at 530.77 eV, corresponding to the C-OH group, confirms its presence. In the composite, the O 1s peaks shifted to higher binding energies, indicating the formation of multiple chemical bonds between Taxol functional groups and MoS_2. This shift reflects a decrease in electron density and an increase in binding energy for the functional groups, evidencing strong interfacial interactions that facilitate efficient interfacial charge transport. Figure S7A compares the N 1s spectra before and after hybridisation with MoS_2. Peaks associated with amino (-NH_2) and amide (-CONH) groups shifted to lower binding energies, suggesting the relatively weak interactions dominated by van der Waals forces or hydrogen bonding rather than covalent bonding. This observation indicates that the hydroxyl group (-OH) is the main functional moieties driving strong chemical interaction with MoS_2, which critically contributes to the improved device performance. Additionally, Figure S7B shows the S 2p spectra shift to lower binding energies after Taxol modification, indicating an increase in electron

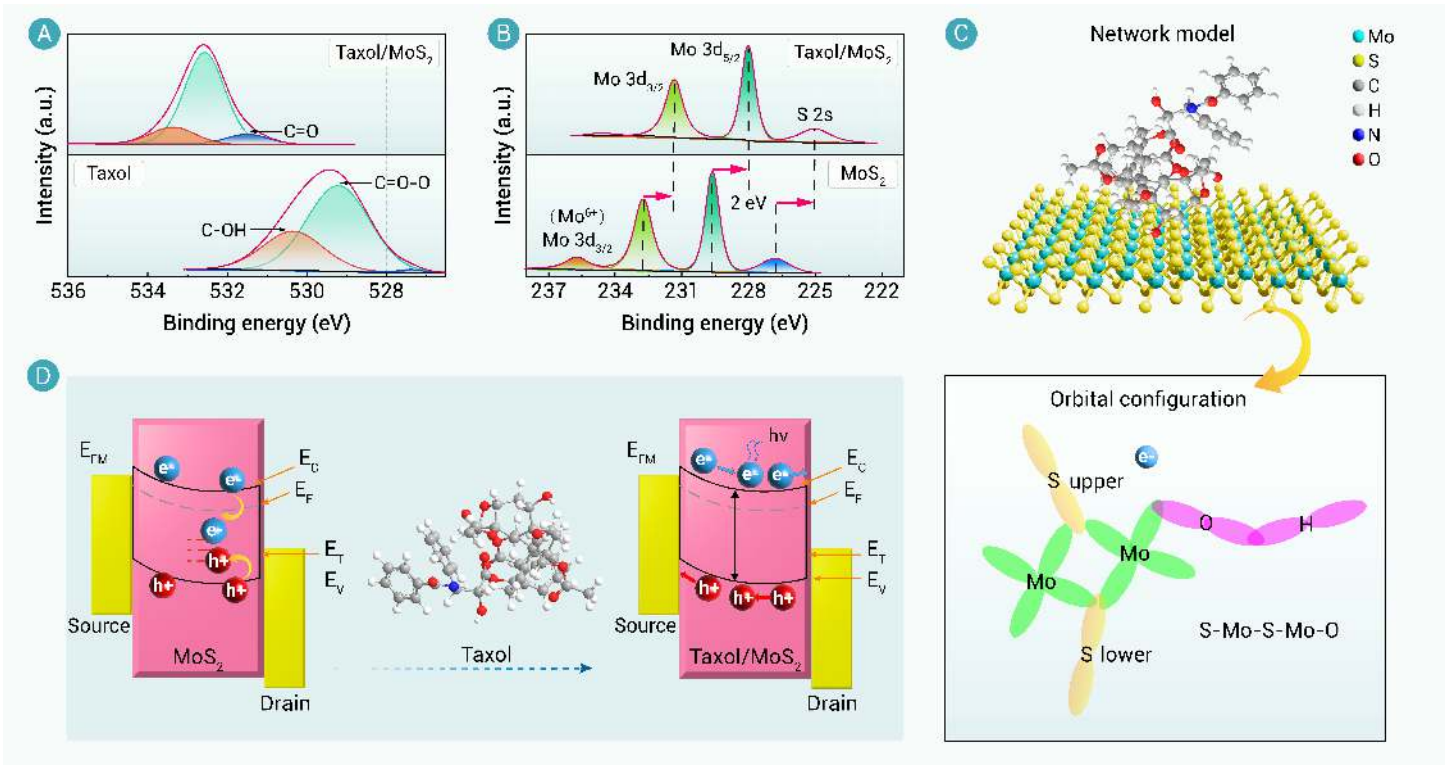

Figure 6. XPS characterisation and interaction mechanism of Taxol/MoS_2. XPS spectra of (A) O 1s and (B) Mo 3d. (C) Schematic illustration of Mo-O bonding. (D) Effect of Taxol modification on the Band Structure of MoS_2.

density in sulfur atoms. Although S and -OH groups rarely form strong covalent bonds, this shift highlights the redistribution of interfacial electron density and further supports the presence of favorable interfacial coupling.

Simultaneously, the Mo $3d_{5/2}$ and Mo $3d_{3/2}$ spectra (Figure 6B) shift to lower binding energies after Taxol modification, indicating electron transfer from the Mo atoms through bonding with the hydroxyl (-OH) group in Taxol. This transfer increases the electron density of Mo atoms, thereby reducing their binding energy and confirming the successful organic modification on MoS_2. Figure 6C schematically illustrates the interfacial process: electrons are injected into MoS_2 via Mo-O bonds at the Taxol/MoS_2 interface, enhancing light absorption and photocurrent generation. Unmodified MoS_2 typically exhibits Mo^{6+} peaks associated with surface defect states, particularly sulfur vacancies. After Taxol modification (Figure 6B), the Mo^{6+} signal is significantly reduced, indicating effective passivation of these defects and the formation of a smoother, more stable surface. Figure 6D further depicts the energy-level alignment before and after Taxol passivation, highlighting how Taxol not only preserves the integrity of the MoS_2 lattice but also repairs surface defects. This defect suppression reduces trap states, mitigates interfacial carrier recombination, and lowers charge trapping effects, thereby explaining the exceptionally low noise levels and enhanced mobility of the Taxol/MoS_2 FETs. In summary, XPS analysis reveals the underlying mechanism of performance enhancement in MoS_2 after Taxol modification. The organic functionalization optimises interfacial charge transport, effectively passivates defects, and markedly improves the optoelectronic properties of MoS_2. These results provide a promising strategy for controlled organic modification and performance tuning of two-dimensional semiconductors.

To further elucidate the passivation effect of hydroxyl adsorption on intrinsic sulfur vacancies in monolayer MoS_2, first-principles density functional theory (DFT) calculations were performed. Several possible adsorption sites were evaluated to determine the most stable configuration of OH bound to monolayer MoS_2, and corresponding computational models were constructed (Figure S8). For comparison, pristine MoS_2 and MoS_2 containing S vacancies were also modelled and fully optimized before electronic structure calculations (Figures 7A-C). The resulting band structures (Figure S9) demonstrate that S vacancies introduce impurity states within the bandgap, disrupting the direct-gap nature of MoS_2. Upon OH adsorption, these defect-induced states largely disappear, restoring the semiconductor to a direct bandgap with a widened gap approaching its intrinsic value. The projected density of states (PDOS, Figure S10) further confirms this effect. Mid-gap impurity peaks vanish after OH adsorption, accompanied by an increase in electron concentration and an overall rise in the density of electronic states. These theoretical results reveal that OH groups effectively passivate S vacancies in MoS_2, eliminating deep-level defect states and thereby improving its intrinsic electronic properties.

In addition, deformation potential (DP) theory was employed to evaluate the carrier transport properties of MoS_2 before and after OH adsorption. Using the calculated deformation potential constants (E_i), elastic constants (C_{ij}), and effective carrier masses (m^*), the acoustic phonon–limited mobilities at 300 K were determined and are summarized in Tables S1–S2 (with detailed derivations shown in Figures S11–S13). For pristine monolayer MoS_2, the calculated electron mobilities are 77.97 $cm^2\ V^{-1}\ s^{-1}$ along the x-direction and 68.14 $cm^2\ V^{-1}\ s^{-1}$ along the y-direction. In contrast, hole mobilities are approximately three times higher, reaching 198.70 $cm^2\ V^{-1}\ s^{-1}$ and 174.78 $cm^2\ V^{-1}\ s^{-1}$ along the x- and y-directions, respectively. These calculated electron mobilities are consistent with reported experimental values.[69,70] The higher hole mobility is attributed to the smaller valence-band deformation potential constant compared with that of the conduction band. In the presence of S vacancies, electron mobilities decrease to 57.15 $cm^2\ V^{-1}\ s^{-1}$ (x-direction) and 51.49 $cm^2\ V^{-1}\ s^{-1}$ (y-direction), while hole mobilities are reduced to 157.45 $cm^2\ V^{-1}\ s^{-1}$ and 143.51 $cm^2\ V^{-1}\ s^{-1}$, respectively. Following OH adsorption, the transport properties are significantly restored: electron mobilities increase to 61.71 $cm^2\ V^{-1}\ s^{-1}$ (x-direction) and 57.49 $cm^2\ V^{-1}\ s^{-1}$ (y-direction), while hole mobilities recover to 198.40 $cm^2\ V^{-1}\ s^{-1}$ and 173.76 $cm^2\ V^{-1}\ s^{-1}$ (Figures 7D-E). Overall, these results demonstrate that OH adsorption effectively passivates intrinsic sulfur vacancies in monolayer MoS_2, reconstructs local edge structures, and enhances carrier mobility. This improvement in charge transport highlights the potential of OH-functionalized MoS_2 for high-performance photodetector applications.

CONCLUSION

In conclusion, we successfully fabricated n-type and p-type MoS_2 using the molten salt-assisted CVD method and the sputtering-CVD (CVD two-step

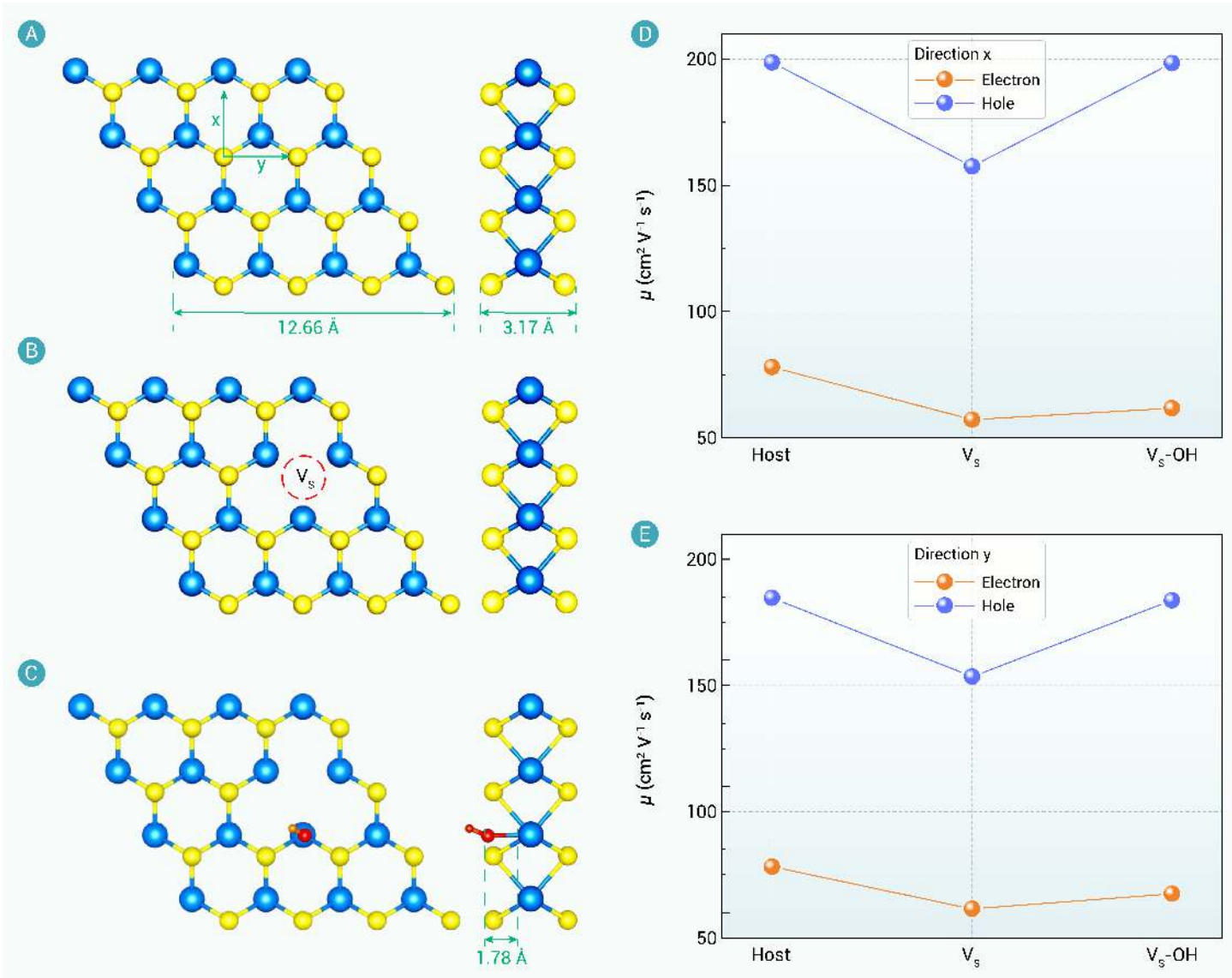

Figure 7. First-principles calculation models (top and side views) and the corresponding variations in carrier mobility (A) Pristine MoS_2 lattice model. (B) S vacancy model; (C) OH adsorption model. (D) Calculated Mobility in the x-direction for different models. (E) Calculated mobility in the y-direction for different models.

method), respectively. Taxol molecules were then employed to repair intrinsic defects in 2D MoS_2. Comprehensive characterization and optoelectronic measurements demonstrate that Taxol enables non-destructive interfacial modification of n- and p-type MoS_2, providing a potentially universal strategy for the gentle functionalization of two-dimensional materials. The hydroxyl groups in Taxol form bonds with Mo atoms in MoS_2, facilitating efficient electron injection and markedly enhancing the photoresponse. Furthermore, Taxol modification exhibits a pronounced defect-passivation effect, suppressing carrier recombination at the interface and reducing noise power spectral density. Therefore, compared with the work of predecessors, the mobility of n- and p-type MoS_2 FETs modified by Taxol in this work has increased significantly (19.90 and 14.70 $cm^2\ V^{-1}\ s^{-1}$ respectively), and their detectivities have also increased to 1.46×10^{12} and 6.25×10^{10} Jones respectively (Table S3).[71-80] This work thus establishes an interfacial modification strategy using Taxol molecules for defect passivation in 2D semiconductors, offering an effective route to tune their electronic and optoelectronic properties for high-performance device applications.

REFERENCES

1. Zhang W., Qiu F., Li Y. et al. (2021). Lattice defect engineering enables performance-enhanced MoS_2 photodetection through a paraelectric $BaTiO_3$ dielectric. *ACS Nano* **15**:13370–13379. DOI:10.1021/acsnano.1c03402
2. Hu T., Zhang R., Li J.P. et al. (2022). Photodetectors based on two-dimensional MoS_2 and its assembled heterostructures. *Chip* **1**:100017. DOI:10.1016/j.chip.2022.100017
3. Purbayanto M.A.K., Chandel M., Birowska M. et al. (2023). Optically active Mxenes in van der Waals heterostructures. *Adv. Mater.* **35**:2301850. DOI:10.1002/adma.202301850
4. Lin H., Zhang Z.F., Zhang H.H. et al. (2022). Engineering van der Waals materials for advanced metaphotonics. *Chem. Rev.* **122**:15204–15355. DOI:10.1021/acs.chemrev.2c00048
5. Liu C.S., Chen H.W., Wang S.Y. et al. (2020). Two-dimensional materials for next-generation computing technologies. *Nat. Nanotechnol.* **15**:545–557. DOI:10.1038/s41565-020-0724-3
6. Zhang Y., Yang H., Wei D. et al. (2021). Mitochondria-targeted nanoparticles in treatment of neurodegenerative diseases. *Exploration* **1**:20210115. DOI:10.1002/EXP.20210115
7. Wang J., Chen D., Huang W. et al. (2023). Aptamer-functionalized Field-Effect Transistor biosensors for disease diagnosis and environmental monitoring. *Exploration* **3**:20210027. DOI:10.1002/EXP.20210027
8. Nan H. Y., Wang Z. L., Wang W. H. et al. (2014). Strong photoluminescence enhancement of MoS_2 through defect engineering and oxygen bonding. *ACS Nano* **8**:5738–5745. DOI:10.1021/nn500532f
9. Ni Z.H., Ponomarenko L.A., Nair R.R. et al. (2010). On resonant scatterers as a factor limiting carrier mobility in graphene. *Nano Lett.* **10**:3868–3872. DOI:10.1021/nl101399r
10. Jiang J., Yang P., Liou J.J. et al. (2022). Defect engineering of two-dimensional materials towards next-generation electronics and optoelectronics. *Nano Res.* **16**:3104–3124. DOI:10.1007/s12274-022-5016-9
11. Xu Z.H., He M., Wu Q.K. et al. (2023). Ultrafast charge transfer 2D MoS_2/organic

heterojunction for sensitive photodetector. *Adv. Sci.* **10**:2207743. DOI:10.1002/advs.202207743
12. Wang C., Cusin L., Ma C. et al. (2024). Enhancing the carrier transport in monolayer MoS_2 through interlayer coupling with 2D covalent organic frameworks. *Adv. Mater.* **36**:2305882. DOI:10.1002/adma.202305882
13. Han J.Y., Wang F.K., Han S. et al. (2022). Recent progress in 2D inorganic/organic charge transfer heterojunction photodetectors. *Adv. Funct. Mater.* **32**:2205150. DOI:10.1002/adfm.202205150
14. Zhao B.L., Gan Z.Y., Johnson M. et al. (2021). 2D van der Waals heterojunction of organic and inorganic monolayers for high responsivity phototransistors. *Adv. Funct. Mater.* **31**:2105444. DOI:10.1002/adfm.202105444
15. Xu X.M., Lou Z.R., Cheng S.M. et al. (2021). Van der Waals organic/inorganic heterostructures in the two-dimensional limit. *Chem.* **7**:2989–3026. DOI:10.1016/j.chempr.2021.08.013
16. Park S., Mutz N., Kovalenko S.A. et al. (2021). Type-I energy level alignment at the ptcda—monolayer MoS_2 interface promotes resonance energy transfer and luminescence enhancement. *Adv. Sci.* **8**:2100215. DOI:10.1002/advs.202100215
17. Yang F.X., Cheng S.S., Zhang X.T. et al. (2018). 2D organic materials for optoelectronic applications. *Adv. Mater.* **30**:1702415. DOI:10.1002/adma.201702415
18. Oyedele A.D., Rouleau C.M., Geohegan D.B. et al. (2018). The growth and assembly of organic molecules and inorganic 2D materials on graphene for van der Waals heterostructures. *Carbon* **131**:246–257. DOI:10.1016/j.carbon.2018.02.020
19. Zhang X.K., Liao Q.L., Liu S. et al. (2017). Poly(4-styrenesulfonate)-induced sulfur vacancy self-healing strategy for monolayer MoS_2 homojunction photodiode. *Nat. Commun.* **8**:15881. DOI:10.1038/ncomms15881
20. Huang Y., Zhuge F.W., Hou J.X. et al. (2018). Van der Waals coupled organic molecules with monolayer MoS_2 for fast response photodetectors with gate-tunable responsivity. *ACS Nano* **12**:4062–4073. DOI:10.1021/acsnano.8b02380
21. Hong J.H., Jin C.H., Yuan J. et al. (2017). Atomic defects in two-dimensional materials: From single-atom spectroscopy to functionalities in opto-/electronics, nanomagnetism, and catalysis. *Adv. Mater.* **29**:1606434. DOI:10.1002/adma.201606434
22. Huang T., Ding J.F., Liu Z.R. et al. (2022). Insight into the underlying competitive mechanism for the shift of the charge neutrality point in a trilayer-graphene field-effect transistor. *eScience* **2**:319–328. DOI:10.1016/j.esci.2022.03.005
23. Wang X.W., Wang B.L., Zhang Q.H. et al. (2021). Grain-boundary engineering of monolayer MoS_2 for energy-efficient lateral synaptic devices. *Adv. Mater.* **33**:2102435. DOI:10.1002/adma.202102435
24. Li H., Zhang N., Yang J. et al. (2025). Surface modification technologies for promoting the widespread use and recycling of carbon fibers in the construction industry. *Innov. Mater.* **3**:100149. DOI:10.59717/j.xinn-mater.2025.100149
25. Park J.H., Sanne A., Guo Y.Z. et al. (2017). Defect passivation of transition metal dichalcogenides via a charge transfer van der Waals interface. *Sci. Adv.* **3**:e1701661. DOI:10.1126/sciadv.1701661
26. Kwon S., Jeong D.Y., Hong C. et al. (2022). Exciton transfer at heterointerfaces of MoS_2 monolayers and fluorescent molecular aggregates. *Adv. Sci.* **9**:2201875. DOI:10.1002/advs.202201875
27. Wang Y., Gali S.M., Slassi A. et al. (2020). Collective dipole-dominated doping of monolayer MoS_2: Orientation and magnitude control via the supramolecular approach. *Adv. Funct. Mater.* **30**:2002846. DOI:10.1002/adfm.202002846
28. Feng Q.S., Sun Y., Li Y.Z. et al. (2021). Highly photoluminescent monolayer MoS_2 and WS_2 achieved via superacid assisted vacancy reparation and doping strategy. *Laser Photon. Rev.* **15**:2170064. DOI:10.1002/lpor.202100104
29. Zhao Y.D., Bertolazzi S. and Samorì P. (2019). A universal approach toward light-responsive two-dimensional electronics: Chemically tailored hybrid van der Waals heterostructures. *ACS Nano* **13**:4814–4825. DOI:10.1021/acsnano.9b01716
30. Ji H.G., Solís-Fernández P., Yoshimura D. et al. (2019). Chemically tuned p- and n-Type WSe_2 monolayers with high carrier mobility for advanced electronics. *Adv. Mater.* **31**:1903613. DOI:10.1002/adma.201903613
31. Kim J.K., Cho K., Jang J. et al. (2021). Molecular dopant-dependent charge transport in surface-charge-transfer-doped tungsten diselenide field effect transistors. *Adv. Mater.* **33**:2101598. DOI:10.1002/adma.202101598
32. Wang C., de Oliveira R.F., Jiang K.Y. et al. (2022). Boosting the electronic and catalytic properties of 2D semiconductors with supramolecular 2D hydrogen- bonded superlattices. *Nat. Commun.* **13**:510. DOI:10.1038/s41467-022-28116-y
33. Chu J.Y., Liu Z.R., Liu P.D. et al. (2024). Synergistic effect of graphene enhances the responsivity of hybrid perovskite photodetector. *Cell Rep. Phys. Sci.* **5**:102054. DOI:10.1016/j.xcrp.2024.102054
34. Joo P., Jo K., Ahn G. et al. (2014). Functional polyelectrolyte nanospaced MoS_2 multilayers for enhanced photoluminescence. *Nano Lett.* **14**:6456–6462. DOI:10.1021/nl502883a
35. Luo Y., Lu H.Q., Huang J.W. et al. (2024). A molecular coordination strategy for regulating the interface of MoS_2 field effect transistors. *J. Am. Chem. Soc.* **146**:9709–9720. DOI:10.1021/jacs.3c13696
36. Duan R., Qi W.H., Tang K.W. et al. (2025). Sub-nano cluster decoration for the manipulation of the photogenerated carrier behavior of MoS_2. *InfoMat* **7**:e12610. DOI:10.1002/inf2.12610
37. Ketchum R.E.B., Gibson D.M. (1995). A novel method of isolating taxanes from cell suspension cultures of yew (taxus spp.). *J. Liq. Chromatography* **18**:1093–1111. DOI:10.1080/10826079508009278
38. Petrov R.A., Maklakova S.Y., Ivanenkov Y.A. et al. (2018). Synthesis and biological evaluation of novel mono- and bivalent ASGP-R-targeted drug-conjugates. *Bioorg. Med. Chem. Lett.* **28**:382–387. DOI:10.1016/j.bmcl.2017.12.032
39. Jennewein S., Croteau R. (2001). Taxol: Biosynthesis, molecular genetics, and biotechnological applications. *Appl. Microbiol. Biotechnol.* **57**:13–19. DOI:10.1007/s002530100757
40. Choudhary N., Park J., Hwang J.Y. et al. (2014). Growth of large-scale and thickness-modulated MoS_2 nanosheets. *ACS Appl. Mater. Interfaces* **6**:21215–21222. DOI:10.1021/am506198b
41. Zhou J.D., Lin J.H., Huang X.W. et al. (2018). A library of atomically thin metal chalcogenides. *Nature* **556**:355–359. DOI:10.1038/s41586-018-0008-3
42. Garg P., Balachandran S., Adlakha I. et al. (2018). Revealing the role of nitrogen on hydride nucleation and stability in pure niobium using first-principles calculations. *Supercond. Sci. Technol.* **31**:115007. DOI:10.1088/1361-6668/aae147
43. Kresse, Furthmuller (1996). Efficient iterative schemes for Ab initio total-energy calculations using a plane-wave basis set. *Phys. Rev. B* **54**:11169-11186. DOI:10.1103/PhysRevB.54.11169.
44. Jiang Y., Liu P., Wang S. et al. (2025). Compensation effect enables high-mobility in Te-doped gallium antimonide. *Inf. Funct. Mater.* **2**:93–101. DOI:10.1002/ifm2.30
45. Perdew, Burke, Ernzerhof (1996). Generalized gradient approximation made simple. *Phys. Rev. Lett.* **77**:3865-3868. DOI:10.1103/PhysRevLett.77.3865.
46. Perdew, Burke, Wang (1996). Generalized gradient approximation for the exchange-correlation hole of a many-electron system. *Phys. Rev. B* **54**:16533-16539. DOI:10.1103/PhysRevB.54.16533.
47. Grimme S., Ehrlich S., Goerigk L. (2011). Effect of the damping function in dispersion corrected density functional theory. *J. Comput. Chem.* **32**:1456–1465. DOI:10.1002/jcc.21759
48. Zhang W., Zou G.F., Choi J.H. (2020). Adsorption behavior of the hydroxyl radical and its effects on monolayer MoS_2. *ACS Omega* **5**:1982–1986. DOI:10.1021/acsomega.9b03837
49. Bardeen J., Shockley W. (1950). Deformation potentials and mobilities in non-polar crystals. *Phys. Rev.* **80**:72–80. DOI:10.1103/PhysRev.80.72
50. Feng S., Liu C., Zhu Q.B. et al. (2021). An ultrasensitive molybdenum-based double-heterojunction phototransistor. *Nat. Commun.* **12**:4094. DOI:10.1038/s41467-021-24397-x
51. Wang F., Zhang T., Xie R.Z. et al. (2023). How to characterize figures of merit of two-dimensional photodetectors. *Nat. Commun.* **14**:2224. DOI:10.1038/s41467-023-37635-1
52. Li H., Zhang Q., Yap C.C.R. et al. (2012). From bulk to monolayer MoS_2: Evolution of raman scattering. *Adv. Funct. Mater.* **22**:1385–1390. DOI:10.1002/adfm.201102111
53. Zhan Y.J., Liu Z., Najmaei S. et al. (2012). Large-area vapor-phase growth and characterization of MoS_2 atomic layers on a SiO_2 substrate. *Small* **8**:966–971. DOI:10.1002/smll.201102654
54. Zeng Z.Y., Yin Z.Y., Huang X. et al. (2011). Single-layer semiconducting nanosheets: High-yield preparation and device fabrication. *Angew. Chem. Int. Edit.* **50**:11093–11097. DOI:10.1002/anie.201106004
55. Radisavljevic B., Radenovic A., Brivio J. et al. (2011). Single-layer MoS_2 transistors. *Nat. Nanotechnol.* **6**:147–150. DOI:10.1038/nnano.2010.279
56. Fang Y.J., Armin A., Meredith P. et al. (2019). Accurate characterization of next-generation thin-film photodetectors. *Nat. Photonics* **13**:1–4. DOI:10.1038/s41566-018-0288-z
57. Tu L.Q., Cao R.R., Wang X.D. et al. (2020). Ultrasensitive negative capacitance phototransistors. *Nat. Commun.* **11**:101. DOI:10.1038/s41467-019-13769-z
58. Wang J.B., Chen S.C., Yin Z.G. et al. (2020). Broadband organic photodetectors based on ternary blend active layers with enhanced and spectrally flat response. *J. Mater. Chem. C* **8**:14049–14055. DOI:10.1039/d0tc02708a
59. Wang J.B., Liu Z.Y., Zhu T.Q. et al. (2024). Strategies for achieving high-performance photomultiplication-type organic photodetectors and their promising applications. *Nano Energy* **132**:110399. DOI:10.1016/j.nanoen.2024.110399
60. Yuan G.W., Lin D.J., Wang Y. et al. (2020). Proton-assisted growth of ultra-flat graphene films. *Nature* **577**:204–208. DOI:10.1038/s41586-019-1870-3
61. Lu Z.Y., Chen Y., Dang W.Q. et al. (2023). Wafer-scale high-K dielectrics for two-dimensional circuits via van der Waals integration. *Nat. Commun.* **14**:2340. DOI:10.1038/s41467-023-37887-x
62. Zeng D.B., Zhang Z.Y., Xue Z.Y. et al. (2024). Single-crystalline metal-oxide dielectrics for top-gate 2D transistors. *Nature* **632**:788–794. DOI:10.1038/s41586-024-07786-2
63. Huang F.B., Liu C.X., Yang Q.Y. et al. (2025). Lead-based perovskites significantly suppress dark currents toward high-performance multilayer SnS_2/perovskite photodetectors. *ACS Nano* **19**:10989–11000. DOI:10.1021/acsnano.4c16539
64. Huang F.B., Yang Q.Y., Sun Y.Y. et al. (2025). Insight into the effect of h-BN modification on the performance of MoS_2 phototransistors with van der Waals contacts. *ACS Appl. Nano Mater.* **8**:5805–5814. DOI:10.1021/acsanm.5c00540
65. Huang F.B., Chen J.H., Du C.Y. et al. (2022). Mechanically exfoliated few-layer SnS_2 and integrated van der Waals electrodes for ultrahigh responsivity phototransistors. *ACS Appl. Electron. Mater.* **4**:5333–5339. DOI:10.1021/acsaelm.2c01010
66. Liu P.D., Zhang X., Zhang B.L. et al. (2025). Molecular engineering enables high-

performance hybrid perovskite photodetector. *Chip* **4**:100125. DOI:10.1016/j.chip.2024.100125
67. Liu Z.R., Jiang Y.K., Chu J.Y. et al. (2025). Mitigating dielectric confinement effect for ultra-high gain in quasi-2D ruddlesden-popper perovskite photodetectors. *Adv. Opt. Mater.* **13**:e01145. DOI:10.1002/adom.202501145
68. Shin W., Byeon J., Koo R.H. et al. (2024). Toward ideal low-frequency noise in monolayer CVD MoS_2 FETs: influence of van der Waals junctions and sulfur vacancy management. *Adv. Sci.* **11**:2307196. DOI:10.1002/advs.202307196
69. Yu S., Xiong H.D., Eshun K. et al. (2015). Phase transition, effective mass and carrier mobility of MoS_2 monolayer under tensile strain. *Appl. Surf. Sci.* **325**:27–32. DOI:10.1016/j.apsusc.2014.11.079
70. Cai Y.Q., Zhang G., Zhang Y.W. (2014). Polarity-reversed robust carrier mobility in monolayer MoS_2 nanoribbons. *J. Am. Chem. Soc.* **136**:6269–6275. DOI:10.1021/ja4109787
71. Long M., Wang P., Fang H. et al. (2019). Progress, challenges, and opportunities for 2D material based photodetectors. *Adv. Funct. Mater.* **29**:1803807. DOI:10.1002/adfm.201803807
72. Wu H.L., Si H.N., Zhang Z.H. et al. (2018). All-inorganic perovskite quantum dot-monolayer MoS_2 mixed-dimensional van der Waals heterostructure for ultrasensitive photodetector. *Adv. Sci.* **5**:1801219. DOI:10.1002/advs.201801219
73. Ying H.T., Li X., Wang H.M. et al. (2020). Band structure engineering in MoS_2 based heterostructures toward high-performance phototransistors. *Adv. Opt. Mater.* **8**:2000430. DOI:10.1002/adom.202000430
74. Abidi I.H., Giridhar S.P., Tollerud J.O. et al. (2024). Oxygen driven defect engineering of monolayer MoS_2 for tunable electronic, optoelectronic, and electrochemical devices. *Adv. Funct. Mater.* **34**:2402402. DOI:10.1002/adfm.202402402
75. Liu X.Y., Zhu J.Q., Shan Y.F. et al. (2024). An ultrasensitive and broad-spectrum MoS_2 photodetector with extrinsic response using surrounding homojunction. *Adv. Sci.* **11**:2408299. DOI:10.1002/advs.202408299
76. Wang K., Wang F., Cao Y. et al. (2024). High-performance photodetectors based on suspended ultralong CNTs-MoS_2 heterojunction networks. *Adv. Funct. Mater.* **35**:2421980. DOI:10.1002/adfm.202421980
77. Chu Y.T., Chen P.L., Huang S.H. et al. (2025). All-van-der-Waals heterostructure of MoS_2 grating and InSe flake for spectrally selective polarization-sensitive photodetection in NIR region. *ACS Nano* **19**:18545–18555. DOI:10.1021/acsnano.5c02102
78. Kumar A., Chakkar A.G., Das C. et al. (2025). Self-powered broadband photodetectors based on WS_2-anchored MoS_2 with enhanced responsivity and detectivity. *Small* **21**:2502900. DOI:10.1002/smll.202502900
79. Wang B., Zhang N.N., You J. et al. (2025). Visible-near-infrared wavelength-selective photodetection and imaging based on floating-gate phototransistors. *InfoMat* **7**:e12661. DOI:10.1002/inf2.12661
80. Yi O.Y., Zhang C.Y., Wang J. et al. (2025). Gate-tunable dual-mode optoelectronic device for self-powered photodetector and optoelectronic synapse. *Adv. Sci.* **12**:2416259. DOI:10.1002/advs.202416259

FUNDING AND ACKNOWLEDGMENTS

This work was supported by the National Natural Science Foundation of China (No. 12064047), the Key Program of Yunnan Fundamental Research Projects (No.202201AS070010), the Key Research and Development Program of Yunnan Province (No.202503AA080008), and Science and Technology Projects of Yunnan Universities Serving Key Industries (FWCY-ZNT2025001). The funders had no role in study design, data collection and analysis, decision to publish, or preparation of the manuscript.

DECLARATION OF INTERESTS

The authors declare no competing interests.

DATA AND CODE AVAILABILITY

Data are available from the corresponding author upon reasonable request.

SUPPLEMENTAL INFORMATION

It can be found online at https://doi.org/10.59717/j.xinn-mater.2026.100191.